







**Crystallographically dependent bilinear magnetoelectric resistance in a thin WTe<sub>2</sub> layer**Tian Liu <sup>\*</sup>, Arunesh Roy , Jan Hidding , Homayoun Jafari , Dennis K. de Wal , Jagoda Sławińska, Marcos H. D. Guimarães , and Bart J. van Wees*Zernike Institute for Advanced Materials, Nijenborgh 4, 9747 AG Groningen, The Netherlands*

(Received 24 January 2023; revised 19 July 2023; accepted 20 September 2023; published 6 October 2023)

The recently reported bilinear magnetoelectric resistance (BMR) in novel materials with rich spin textures, such as bismuth selenide (Bi<sub>2</sub>Se<sub>3</sub>) and tungsten ditelluride (WTe<sub>2</sub>), opens new possibilities for probing the spin textures via magnetotransport measurements. By its nature, the BMR effect is directly linked to the crystal symmetry of the materials and its spin texture. Therefore, understanding the crystallographic dependency of the effect is crucial. Here we report the observation of crystallographically dependent BMR in thin WTe<sub>2</sub> layers and explore how it is linked to its spin textures. The linear response measured in first-harmonic signals and the BMR measured in second-harmonic signals are both studied under a wide range of magnitudes and directions of the magnetic field and applied current and at different temperatures. We discover a threefold symmetry contribution of the BMR when current is applied along the *a* axis of the WTe<sub>2</sub> thin layer at 10 K, which is absent when current is applied along the *b* axis.

DOI: [10.1103/PhysRevB.108.165407](https://doi.org/10.1103/PhysRevB.108.165407)**I. INTRODUCTION**

The study of spin dynamics in two-dimensional (2D) materials is promising for both fundamental research and potential industrial applications [1–3]. In particular, the rich spin texture of WTe<sub>2</sub> has high potential for spin-active components in spintronic circuits, as indicated via spin- and angle-resolved photoemission spectroscopy (SR-ARPES) measurements [4–8]. Room temperature spin charge conversion was reported in WTe<sub>2</sub>/graphene heterostructures, and the direction of the generated nonequilibrium spin accumulation can be controlled via geometry design [9–11]. However, the complex nature of the spin structure of WTe<sub>2</sub> still remains largely under-researched, while the material is predicted to be a type-II Weyl semimetal [12–15], hosting novel phenomena such as extremely large magnetoresistance (XMR) [16], the nonlinear Hall effect [17,18], spin momentum locking [19], and the quantum spin Hall effect [20–22].

To unveil the potential of WTe<sub>2</sub> in spintronics, an essential step is to explore its spin texture and the associated spin dynamics under electric field and magnetic field, applied along different crystal axes. Spin-polarized bands of WTe<sub>2</sub> have been measured by SR-ARPES and analyzed with density functional theory (DFT) calculations, and spin-polarized Fermi pockets of WTe<sub>2</sub> have been confirmed [6,7]. As a step further, electrical probing of the spin texture of materials is practical for measuring the direct response of the spin-texture-dependent effects under various experimental conditions and tailored to specific device geometries.

For angle-dependent magnetoresistance (ADMR) measurements in a bulk system, there are two relevant types of measurements which depend on the spin dynamics. The first

type, i.e., spin-accumulation-related ADMR, is measured in the linear response. In the linear response, spin accumulation can be generated by a charge current, e.g., via the spin Hall effect in metallic materials [23] or via the Rashba-Edelstein effect (REE) in systems with *k*-dependent spin textures [24]. While the nonequilibrium spin accumulation is generated by a charge current, the reciprocal process is always present, where the spin current is converted to a charge voltage via the reciprocal effects, e.g., the inverse spin Hall effect [25,26] and the inverse Rashba-Edelstein effect [27,28]. When the spin accumulation is dephased by magnetic fields perpendicular to the direction of the spins, this results in Hanle magnetoresistance (HMR) [29]. Alternatively, the spin accumulation can also be controlled by the interaction with the magnetization of an adjacent layer, and this leads to spin Hall magnetoresistance (SMR) [30,31].

The second type of spin-related ADMR is in the second-order response, where the ADMR is linked to the spin current associated with the charge current instead of spin accumulation, as in second order a net spin current is allowed and it can be modulated by the applied magnetic fields. As a spin current is not allowed in the linear response in the spin-orbit system by time-reversal symmetry, this type of ADMR is not allowed in the first order. An example of the second type of spin-related ADMR is the bilinear magnetoelectric resistance (BMR) [32]. Therefore BMR can be detected by applying a magnetic field, which creates unbalanced opposite spin directions as a result of Zeeman energy splitting, leading to a conversion from the spin current to a charge current.

BMR is a powerful tool to study spin textures of novel materials via electrical transport measurements. One advantage is that the spin texture can be directly probed via magnetotransport measurement in a material itself, without the need of fabricating a heterostructure to include other materials or magnetic contacts for spin injection or detection. It was

<sup>\*</sup>tian.liu@rug.nl

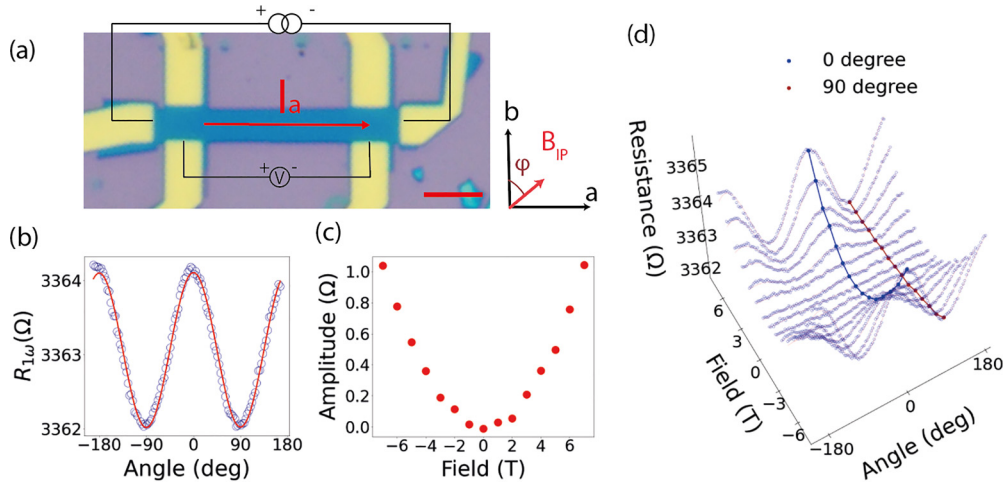


FIG. 1. Device geometry and measurement results for the first-harmonic resistance measured at 300 K. (a) An optical microscope graph and the circuit for the flake resistance measurements along the long edge ( $a$  axis); the scale bar in red at bottom right is  $5 \mu\text{m}$  long. (b) Magnetoresistance in the linear response under in-plane magnetic field at the angle  $\varphi$ . The data are fitted with Eq. (1). (c) The fitted amplitude for magnetic field from  $-7$  to  $7$  T. (d) The full data set of magnetoresistance (MR) under various magnetic fields. The modulation of the MR appears at  $0^\circ$  and  $180^\circ$ , when the field is perpendicular to the current. At  $90^\circ$  ( $-90^\circ$ ) when the field is parallel (antiparallel) to the current, the MR does not scale quadratically with the field.

reported that the BMR scales linearly with both electric field and magnetic field in the second-order response [32]. Focusing on the second order, the resistance of the system can be described as

$$R(I, B) = R_0 + \Delta R \cdot I \cdot B, \quad (1)$$

where  $R_0 = V/I$  is the resistance at zero magnetic field and low current and  $\Delta R$  is the BMR coefficient. The BMR effect is sensitive to the specific crystallographic orientation of the material [32]. It was reported that BMR measurements on  $\text{WTe}_2$  are linked to Fermi surface topology and convexity [33]. However, the crystal-axis-dependent spin texture of  $\text{WTe}_2$  has not yet been revealed via the BMR effect. As the  $bc$  plane is the only mirror plane of the crystal and the  $ac$  plane is not a mirror plane [34], a crystallographically dependent BMR is allowed and expected.

In this paper, we fabricated three  $\text{WTe}_2$  Hall bar devices (samples A, B, and C) with different thicknesses and measured their electronic transport properties. We only present the measurement results of sample A (9-nm  $\text{WTe}_2$  flake on top of  $\text{SiO}_2$ ) in the main text, as it shows the most pronounced ADMR signals. The optical images of the three samples and the measurement results can be found in the Supplemental Material (SM) [35]. The  $\text{WTe}_2$  flakes were exfoliated from orthorhombic  $\text{WTe}_2$  crystals (obtained from HQ Graphene) on  $\text{SiO}_2$  substrates. The exfoliation was performed in a nitrogen atmosphere with  $\text{O}_2 < 0.1$  ppm and  $\text{H}_2\text{O} < 0.5$  ppm. The contacts were designed and written following standard electron-beam lithography procedures. Before depositing Au/Ti contacts (75 nm/5 nm in thickness) on top of the  $\text{WTe}_2$  via an electron-beam evaporation system, mild argon ion milling was performed for 20 s to remove the possible degraded surface of  $\text{WTe}_2$ , as the flake was exposed to air for tens of seconds before loading into the metal deposition system. After the metal deposition, a lift-off procedure was followed, and the sample was immersed in acetone solution

before its loading into a different glove box filled with nitrogen (oxygen level below 0.1%;  $\text{H}_2\text{O}$  level below 2.8 mbar), where the sample was spin coated with poly(methyl methacrylate) (PMMA). Through a standard electron-beam lithography step, a Hall bar shape of the PMMA layer was left on top of the flake, acting as an etching mask. Then the  $\text{WTe}_2$  flake was etched into the Hall bar shape by  $\text{CF}_4$  reactive-ion etching, following the natural exfoliated direction of the samples. For the sample presented in the main text of this paper, the long edge of the flake is aligned with the  $a$  axis of  $\text{WTe}_2$ , as indicated in Fig. 1(a). The crystal orientation was determined by polarized Raman measurements directly on this device, as shown in the SM. After etching, the PMMA mask was removed, and an extra PMMA layer (270 nm thick) was spin coated to protect the sample during sample bonding and electrical measurements.

## II. MEASUREMENTS

In our electrical measurements, we applied AC currents along different crystal axes of  $\text{WTe}_2$  and separate different harmonics via standard lock-in techniques. The voltage response is composed of different orders and is expanded as  $V(t) = R_1 I(t) + R_2 I^2(t) + \dots$  [36], where  $R_i$  is the  $i$ th-order response [37] to the applied AC current  $I(t)$  [38]. We measure the first-harmonic signal (i.e., linear response  $R_{1\omega}$ ) and the second-harmonic signal ( $R_{2\omega}$ ) for both longitudinal voltage (Figs. 1–4) and transverse voltage, as shown in the SM [35]. We focused on longitudinal and transverse resistance measurements on a Hall bar device made from a 9-nm-thick  $\text{WTe}_2$  flake, as a function of the direction and magnitude of the electric and magnetic fields. We also perform similar measurements on the other two samples, which show overall similar results for the linear response. The measurements are shown in the SM [35].

A typical four-terminal longitudinal voltage measurement is shown in Fig. 1(a); in this configuration an AC current

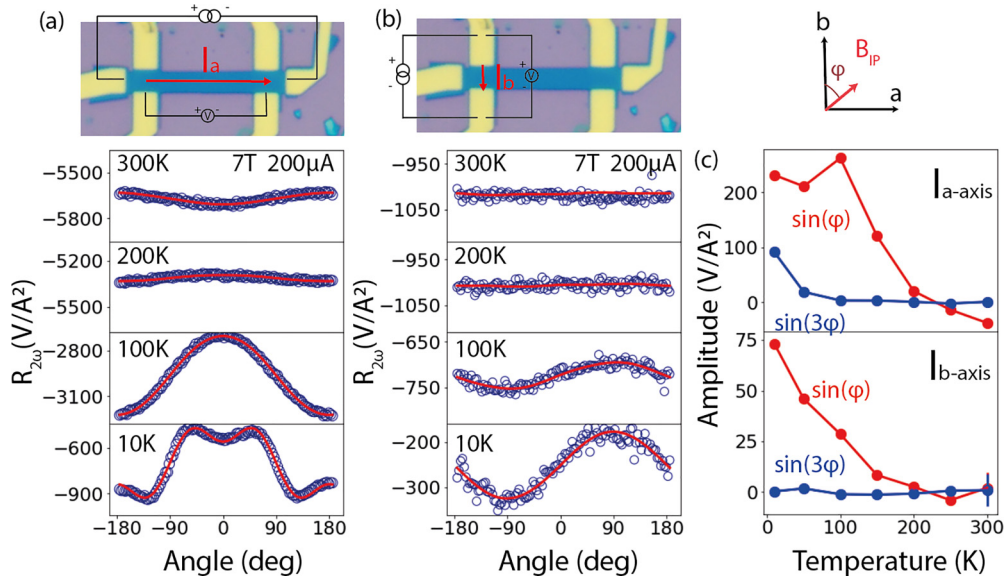


FIG. 2. The second-harmonic longitudinal resistance measurements at different temperatures. (a) Four-terminal longitudinal second-harmonic resistance along the *a* axis. (b) Two-terminal longitudinal second-harmonic resistance along the *b* axis. (c) Fitting amplitudes of  $\sin(\varphi)$  (red) and  $\sin(3\varphi)$  (blue) for the longitudinal second-harmonic resistance with the current along the *a* axis (top panel) and *b* axis (bottom panel). The error bars that are not visible are smaller than the point size.

of 200  $\mu$ A is applied along the *a* axis of WTe<sub>2</sub>. The data were measured at 300 K. When an in-plane magnetic field is applied at an angle  $\varphi$  with respect to *I*, we observe an angle-dependent magnetoresistance (ADMR) which shows a periodicity of 180° in the linear response [Fig. 1(b)]. The measured ADMR is fitted with a sine function:

$$R_{1\omega} = A \sin(2\varphi + \pi) + B, \quad (2)$$

where *A* is the amplitude of the ADMR and *B* is the background resistance. We found that the fitted amplitude *A* depends on the magnetic field quadratically, as shown in Fig. 1(c), which is consistent with the literature [33]. At 7 T, it shows an amplitude  $A = 1.044 \pm 0.008 \Omega$ , and the total modulation of the ADMR ( $2A$ ) is 0.06% of the flake resistance at room temperature. We take a linear background into account during the fitting, which we believe comes from the capacitive couplings in the circuit.

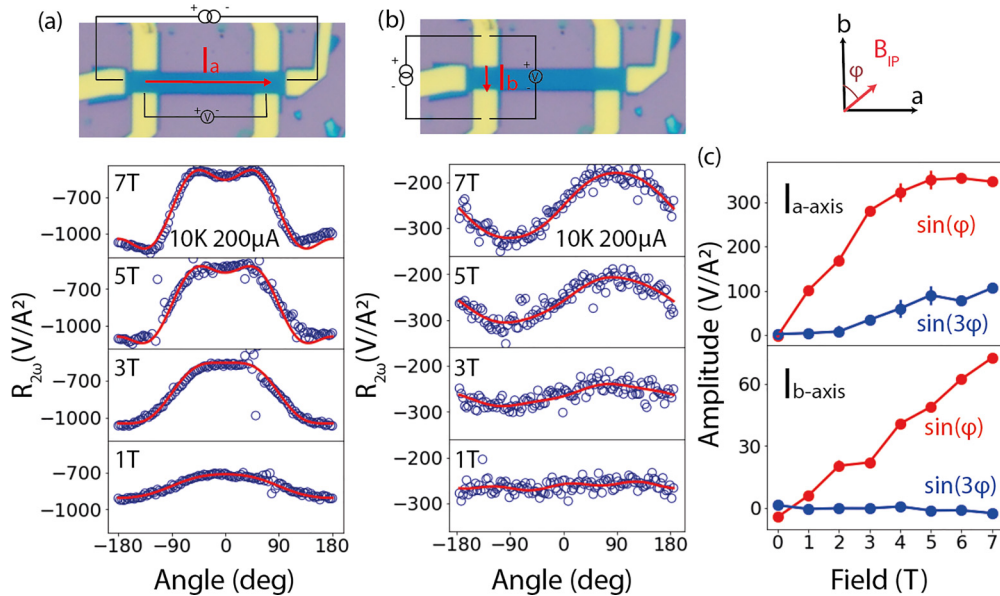


FIG. 3. The second-harmonic longitudinal resistance measurements under different magnetic fields. (a) Four-terminal longitudinal second-harmonic resistance along the *a* axis. (b) Two-terminal longitudinal second-harmonic resistance along the *b* axis. (c) Fitting amplitudes of  $\sin(\varphi)$  (red) and  $\sin(3\varphi)$  (blue) for the longitudinal second-harmonic resistance with the current along the *a* axis (top panel) and *b* axis (bottom panel). When the error bars are not visible, they are smaller than the point size.

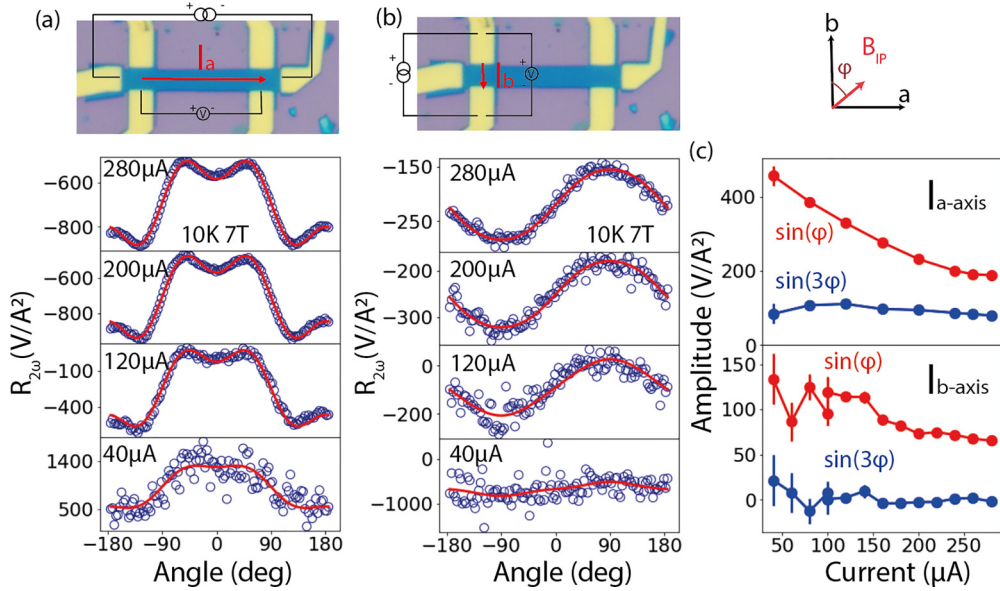


FIG. 4. The second-harmonic longitudinal resistance measurements with different currents. (a) Four-terminal longitudinal second-harmonic resistance along the  $a$  axis. (b) Two-terminal longitudinal second-harmonic resistance along the  $b$  axis. (c) Fitting amplitudes of  $\sin(\varphi)$  (red) and  $\sin(3\varphi)$  (blue) for the longitudinal second-harmonic resistance with the current along the  $a$  axis (top panel) and  $b$  axis (bottom panel). When the error bars are not visible, they are smaller than the point size.

Interestingly, from ADMR measurements under a range of magnetic fields of different magnitudes from  $-7$  to  $7$  T [as shown in Fig. 1(d)], we find that the first-order ADMR is strongly sensitive to the angle between the applied current direction and the magnetic field direction. The ADMR reaches the maximum value and scales quadratically with magnetic field, when the field is perpendicular to the current [as shown by the blue dots for the data measured at  $\varphi = 0^\circ$  in Fig. 1(d)]. There is no quadratic dependence when the field is along the current [as shown by the red dots for the data measured at  $\varphi = 90^\circ$  in Fig. 1(d)], while an almost linear change in the resistance on the field is observed, although it is unclear where the background signal on the field comes from. The ADMR shown in the first-harmonic signal  $R_{1\omega}$  is independent of the crystal axes. These results indicate that the ADMR in this linear response comes from a mechanism which is independent of crystallographic orientations, and this is different from the following discussion of BMR.

A possible explanation for this ADMR at room temperature is the Hanle magnetoresistance (HMR). For HMR, the spin direction, and the corresponding direction component, of the spin accumulation which is perpendicular to the magnetic field is dephased. The effect scales quadratically with the magnetic field. The HMR type of effect generally leads to an increase in the resistance which fits into our observation in Fig. 1(b). However, in special cases, e.g., in the chiral system, the HMR type of effect could also lead to a decrease in the resistance [39]. This quadratic dependence matches with our observation as shown in Fig. 1(c), implying that the spin direction of the spin accumulation is along the current. As a possible explanation for the HMR, we resort to the symmetry analysis. From the symmetry point of view, the 9-nm-thick flake can be associated with space groups 6, 11, or 31, and the applied current is along either the  $a$  axis or  $b$  axis of the crystal. The unconventional spin Hall effects where the

applied current direction, electric field, and spin polarizations are mutually collinear are not allowed by these space groups [40]. Therefore such spin Hall effects are ruled out from the possible origins.

In the SM [35], we also show a reciprocity check for the transverse resistance: After interchanging the current source and the voltage probe, the measurement results are the same. In Eq. (2), a phase “ $\pi$ ” is introduced to make the fitted amplitude positive for the 300-K ADMR. By adding this phase we define this as a positive magnetoresistance, due to the resistance increase while the field is perpendicular to the current.

We now discuss the second-harmonic measurements. The BMR effect is measured via the second-harmonic signals  $R_{2\omega}$ , and it shows strong crystallographic dependence at temperatures below 50 K [deviations from a pure (co)sinusoidal dependence]. Figures 2(a) and 2(b) show measurements for the current applied along the  $a$  axis and  $b$  axis, respectively. Clear differences in the BMR amplitude and periodicity are observed. The transverse  $R_{2\omega}$  is also measured and is shown in the SM [35]. For the longitudinal  $R_{2\omega}$ , in contrast to previous reports [33] where only a  $\sin(\varphi)$  component was observed, here we measured an additional  $\sin(3\varphi)$  component when the current is applied along the  $a$  axis of the  $\text{WTe}_2$  crystal. Our data are fitted by

$$R_{2\omega} = A_1 \sin(\varphi + \pi) + A_2 \sin(3\varphi + \pi/2) + B. \quad (3)$$

$A_1$  is the amplitude for the  $\sin(\varphi)$  part, and  $A_2$  is the amplitude for the  $\sin(3\varphi)$  contribution. A  $\varphi$ -dependent background  $B$  is always present, and it depends on the temperature, the field, and the applied current (see SM [35] for details). A similar equation is used to fit the data which were measured when the current was applied along the  $b$  axis:

$$R_{2\omega} = A_1 \sin(\varphi + \pi/2) + A_2 \sin(3\varphi) + B. \quad (4)$$

Note that here a different phase  $\pi/2$  is used due to a  $\pi/2$  change in the applied current direction. The biggest amplitude  $A_2$  is at 10 K (the lowest measured temperature) when a current is applied along the  $a$  axis, while  $A_1$  saturates for temperatures lower than 100 K. We notice that the  $\sin(3\varphi)$  modulation is similar to the DC transverse resistance measurement from Li *et al.* [41], where the harmonic separation is lacking, and it is not clear whether the  $\sin(3\varphi)$  component is in the linear or nonlinear response. We report this  $\sin(3\varphi)$  contribution in the longitudinal resistance measurement and identify it in the second harmonic.

We also measured the longitudinal  $R_{2\omega}$  for different magnitudes of magnetic field at 10 K for a fixed applied current of 200  $\mu\text{A}$ , as shown in Fig. 3(a) for the current applied along the  $a$  axis and in Fig. 3(b) for the current applied along the  $b$  axis. These data are fitted with Eqs. (3) and (4), respectively, and the fitting amplitudes are plotted in the top and bottom panels of Fig. 3(c). In BMR studies of both  $\text{Bi}_2\text{Se}_3$  [32] and  $\text{WTe}_2$  [33], the effect scales linearly with the field with a periodic angular dependency of  $2\pi$ . We observe similar results, i.e., the linear dependency of the longitudinal BMR on the field, when the current is applied along the  $a$  axis, as shown in the top panel of Fig. 3(c). In this case, no significant  $\sin(3\varphi)$  contribution is observed. This linear dependence of BMR on the field is not observed anymore when the current is applied along the  $b$  axis, especially for the  $\sin(\varphi)$  component. At 10 K and with an applied current of 200  $\mu\text{A}$ , both the  $\sin(\varphi)$  component and the  $\sin(3\varphi)$  component of BMR saturate for fields higher than 5 T.

We also show the current dependence of the BMR in Fig. 4(a) for the current applied along the  $a$  axis and in Fig. 4(b) for the current applied along the  $b$  axis. These data are fitted with Eqs. (3) and (4), respectively, and the results are shown in the top and bottom panels of Fig. 4(c). The BMR  $R_{2\omega}$  is supposed to be constant with the current when it is expressed in units of  $\text{V}/\text{A}^2$  (and it is supposed to be linear with the current when it is in units of ohms). However, we observed a higher BMR signal at low currents, as shown in the top and bottom panels of Fig. 4(c). In the SM [35], we plot measurements with different currents at 10 K without a magnetic field. We found a resistance change of 5% from 20 to 200  $\mu\text{A}$ , and therefore the 50% drop in the amplitude of  $R_{2\omega}$  in the  $a$  axis cannot be explained solely by heating. The amplitude of  $R_{2\omega}$  in Fig. 2 does not highly depend on the temperature when below 100 K either.

### III. DISCUSSION

To give a tentative understanding of our results, in particular the different periodicities of the first-harmonic (linear) response and the second-order BMR, we note that the roles of the magnetic field are different. Similar to the conventional Rashba-Edelstein effect, in the linear response the charge currents induce a shifted distribution which produces a spin accumulation (note that there is no spin current generated in the linear regime). Similar to the inverse REE, the spin accumulation is converted back into a current, which can increase or decrease the resistance. The applied magnetic field, when it is perpendicular to the direction of the spin accumulation, will induce spin precession and thus reduce the spin accumulation.

Thus the resistance will be modified accordingly. Note that the dephasing will be the same when the magnetic field is reversed by  $180^\circ$ ; therefore the resistance modulation in the linear regime will have a  $180^\circ$  periodicity of the magnetic field direction, and the amplitude will depend on  $B^2$ .

The origin of the first-harmonic ADMR remains an open question, i.e., whether it arises from HMR. Future experiments to verify this could use spin-pumping measurements in a yttrium iron garnet (YIG)/ $\text{WTe}_2$  structure, where a pure spin current can be addressed in a more well-defined way, and the spin-to-charge conversion can be separated from the charge-to-spin conversion. This would help in identifying the mechanism of the reported first-harmonic ADMR.

The origin of the second-order BMR is different. Here we can give a tentative explanation by noting that in the nonlinear regime a spin current can be generated. Without a magnetic field there is no symmetry breaking, and no charge current will evolve. However, applying a magnetic field parallel to the spin polarization, an asymmetry can be induced by the Zeeman energy between spins propagating in the positive  $k$  direction and those propagating in the negative  $k$  direction. This will result in a charge current in the second order, whose strength and direction will depend linearly on the magnetic field. However, the details of this mechanism will strongly depend on the specific spin texture. We have calculated the spin texture (as shown in the SM [35]), where the predominant periodicity is  $360^\circ$ . Corresponding to this periodicity, when rotating the magnetic field direction, the BMR periodicity will be  $360^\circ$ . However, we did not find an explanation for the threefold symmetry of the BMR signal at low temperature. This remains to be explored in future research.

The exact calculation of BMR becomes very challenging for multilayer  $\text{WTe}_2$  due to the complication of a finite temperature and numerous spin subbands. Besides the nonzero temperature and the sophisticated spin subbands, we would like to also point out that the spin texture itself could already change its orientation in high magnetic fields (even at around 10 T) and the Zeeman energy could play a role in the measured second-order resistance [42]. Normally, the Zeeman energy will not affect the transport of a 2D system, as the density of states will decrease canceling the lifted speed of charge carriers. However, in a quasi-2D system, the role of Zeeman energy becomes nontrivial. To fully understand the origin of the  $\sin(3\varphi)$  BMR contribution, a dedicated investigation into the microscopic details of thin  $\text{WTe}_2$  is needed for future investigations.

In summary, we report interesting transport measurements on  $\text{WTe}_2$  devices with a Hall bar geometry. The first-harmonic ADMR is sensitive to the magnetic field perpendicular to the applied current, and it is crystal axis independent. The origin of this ADMR needs to be explored. We also observe a second-harmonic ADMR originating from the BMR, which is strongly crystallographically dependent. A  $\sin(3\varphi)$  contribution of the BMR is reported, and we believe that it is linked to the spin texture of the 9-nm  $\text{WTe}_2$  thin flake. These observations are relevant for understanding the spin texture and the nature of spin current dynamics in thin  $\text{WTe}_2$  layers and pave the way for further spintronic applications utilizing the rich spin texture in  $\text{WTe}_2$  and other relevant 2D materials.

## ACKNOWLEDGMENTS

The authors thank Prof. S. Dash and Dr. B. Zhao for helpful discussions on the device fabrication. The authors thank Prof. M. Loi and E. Tekelenburg for granting access to their polarized Raman setup and for necessary help. The authors would also like to thank Dr. A. Kaverzin for the discussion on the resistance calculation and Dr. Julian Peiro and Dr. Si Chen for interesting discussions which sparked the initial idea for this project. This project has

received funding from the Dutch Research Council on Matter (FOM, now known as NWO-I) as part of the Netherlands Organization for Scientific Research (NWO), the European Union's Horizon 2020 research and innovation program under Grant Agreements No. 696656 and No. 785219 (Graphene Flagship Core 1, Core 2, and Core 3), and Zernike Institute for Advanced Materials. M.H.D.G. acknowledges support from NWO Grant No. STU.019.014. J.S. acknowledges support from the Rosalind Franklin Fellowship from the University of Groningen.

- 
- [1] A. Avsar, H. Ochoa, F. Guinea, B. Özyilmaz, B. J. van Wees, and I. J. Vera-Marun, Colloquium: Spintronics in graphene and other two-dimensional materials, *Rev. Mod. Phys.* **92**, 021003 (2020).
- [2] Q. H. Wang, K. Kalantar-Zadeh, A. Kis, J. N. Coleman, and M. S. Strano, Electronics and optoelectronics of two-dimensional transition metal dichalcogenides, *Nat. Nanotechnol.* **7**, 699 (2012).
- [3] S. Manzeli, D. Ovchinnikov, D. Pasquier, O. V. Yazyev, and A. Kis, 2D transition metal dichalcogenides, *Nat. Rev. Mater.* **2**, 17033 (2017).
- [4] D. Hsieh, Y. Xia, L. Wray, D. Qian, A. Pal, J. Dil, J. Osterwalder, F. Meier, G. Bihlmayer, C. Kane, Y. S. Hor, R. J. Cava, and M. Z. Hasan, Observation of unconventional quantum spin textures in topological insulators, *Science* **323**, 919 (2009).
- [5] D. Hsieh, Y. Xia, D. Qian, L. Wray, F. Meier, J. Osterwalder, L. Patthey, J. G. Checkelsky, N. Ong, A. V. Fedorov, H. Lin, A. Bansil, D. Grauer, Y. S. Hor, R. J. Cava, and M. Z. Hasan, A tunable topological insulator in the spin helical Dirac transport regime, *Nature (London)* **460**, 1101 (2009).
- [6] B. Feng, Y.-H. Chan, Y. Feng, R.-Y. Liu, M.-Y. Chou, K. Kuroda, K. Yaji, A. Harasawa, P. Moras, A. Barinov, W. Malaeb, C. Bareille, T. Kondo, S. Shin, F. Komori, T.-C. Chiang, Y. Shi, and I. Matsuda, Spin texture in type-II Weyl semimetal  $WTe_2$ , *Phys. Rev. B* **94**, 195134 (2016).
- [7] P. K. Das, D. Di Sante, I. Vobornik, J. Fujii, T. Okuda, E. Bruyer, A. Gyenis, B. E. Feldman, J. Tao, R. Ciancio, G. Rossi, M. N. Ali, S. Picozzi, A. Yazdani, G. Panaccione, and R. J. Cava, Layer-dependent quantum cooperation of electron and hole states in the anomalous semimetal  $WTe_2$ , *Nat. Commun.* **7**, 10847 (2016); Erratum: Layer-dependent quantum cooperation of electron and hole states in the anomalous semimetal  $WTe_2$ , **7**, 11355 (2016); Author Correction: Layer-dependent quantum cooperation of electron and hole states in the anomalous semimetal  $WTe_2$ , **10**, 648 (2019).
- [8] J. Jiang, F. Tang, X. C. Pan, H. M. Liu, X. H. Niu, Y. X. Wang, D. F. Xu, H. F. Yang, B. P. Xie, F. Q. Song, P. Dudin, T. K. Kim, M. Hoesch, P. K. Das, I. Vobornik, X. G. Wan, and D. L. Feng, Signature of strong spin-orbital coupling in the large nonsaturating magnetoresistance material  $WTe_2$ , *Phys. Rev. Lett.* **115**, 166601 (2015).
- [9] B. Zhao, D. Khokhriakov, Y. Zhang, H. Fu, B. Karpiak, A. M. Hoque, X. Xu, Y. Jiang, B. Yan, and S. P. Dash, Observation of charge to spin conversion in Weyl semimetal  $WTe_2$  at room temperature, *Phys. Rev. Res.* **2**, 013286 (2020).
- [10] B. Zhao, B. Karpiak, D. Khokhriakov, A. Johansson, A. M. Hoque, X. Xu, Y. Jiang, I. Mertig, and S. P. Dash, Unconventional charge-spin conversion in Weyl-semimetal  $WTe_2$ , *Adv. Mater.* **32**, 2000818 (2020).
- [11] B. Zhao, A. M. Hoque, D. Khokhriakov, B. Karpiak, and S. P. Dash, Charge-spin conversion signal in  $WTe_2$  van der Waals hybrid devices with a geometrical design, *Appl. Phys. Lett.* **117**, 242401 (2020).
- [12] A. A. Soluyanov, D. Gresch, Z. Wang, Q. Wu, M. Troyer, X. Dai, and B. A. Bernevig, Type-II Weyl semimetals, *Nature (London)* **527**, 495 (2015).
- [13] P. Li, Y. Wen, X. He, Q. Zhang, C. Xia, Z.-M. Yu, S. A. Yang, Z. Zhu, H. N. Alshareef, and X.-X. Zhang, Evidence for topological type-II Weyl semimetal  $WTe_2$ , *Nat. Commun.* **8**, 2150 (2017).
- [14] Y. Wang, E. Liu, H. Liu, Y. Pan, L. Zhang, J. Zeng, Y. Fu, M. Wang, K. Xu, Z. Huang, Z. Wang, H.-Z. Lu, D. Xing, B. Wang, X. Wan, and F. Miao, Gate-tunable negative longitudinal magnetoresistance in the predicted type-II Weyl semimetal  $WTe_2$ , *Nat. Commun.* **7**, 13142 (2016).
- [15] Y.-Y. Lv, X. Li, B.-B. Zhang, W. Y. Deng, S.-H. Yao, Y. Chen, J. Zhou, S.-T. Zhang, M.-H. Lu, L. Zhang, M. Tian, L. Sheng, and Y. F. Chen, Experimental observation of anisotropic Adler-Bell-Jackiw anomaly in type-II Weyl semimetal  $WTe_{1.98}$  crystals at the quasiclassical regime, *Phys. Rev. Lett.* **118**, 096603 (2017).
- [16] M. N. Ali, J. Xiong, S. Flynn, J. Tao, Q. D. Gibson, L. M. Schoop, T. Liang, N. Haldolaarachchige, M. Hirschberger, N. P. Ong, and R. J. Cava, Large, non-saturating magnetoresistance in  $WTe_2$ , *Nature (London)* **514**, 205 (2014).
- [17] K. Kang, T. Li, E. Sohn, J. Shan, and K. F. Mak, Nonlinear anomalous Hall effect in few-layer  $WTe_2$ , *Nat. Mater.* **18**, 324 (2019).
- [18] Q. Ma, S.-Y. Xu, H. Shen, D. MacNeill, V. Fatemi, T.-R. Chang, A. M. Mier Valdivia, S. Wu, Z. Du, C.-H. Hsu, S. Fang, Q. D. Gibson, K. Watanabe, T. Taniguchi, R. J. Cava, E. Kaxiras, H.-Z. Lu, H. Lin, L. Fu, N. Gedik *et al.*, Observation of the nonlinear Hall effect under time-reversal-symmetric conditions, *Nature (London)* **565**, 337 (2019).
- [19] P. Li, W. Wu, Y. Wen, C. Zhang, J. Zhang, S. Zhang, Z. Yu, S. A. Yang, A. Manchon, and X.-x. Zhang, Spin-momentum locking and spin-orbit torques in magnetic nano-heterojunctions

- composed of Weyl semimetal  $\text{WTe}_2$ , *Nat. Commun.* **9**, 3990 (2018).
- [20] B. A. Bernevig and S.-C. Zhang, Quantum spin Hall effect, *Phys. Rev. Lett.* **96**, 106802 (2006).
- [21] H. Wu, L. Huang, C. Fang, B. S. Yang, C. H. Wan, G. Q. Yu, J. F. Feng, H. X. Wei, and X. F. Han, Magnon valve effect between two magnetic insulators, *Phys. Rev. Lett.* **120**, 097205 (2018).
- [22] S. Tang, C. Zhang, D. Wong, Z. Pedramrazi, H.-Z. Tsai, C. Jia, B. Moritz, M. Claassen, H. Ryu, S. Kahn, J. Jiang, H. Yan, M. Hashimoto, D. Lu, R. G. Moore, C.-C. Hwang, C. Hwang, Z. Hussain, Y. Chen, M. M. Ugeda *et al.*, Quantum spin Hall state in monolayer  $1\text{T}'\text{-WTe}_2$ , *Nat. Phys.* **13**, 683 (2017).
- [23] J. E. Hirsch, Spin Hall effect, *Phys. Rev. Lett.* **83**, 1834 (1999).
- [24] V. M. Edelstein, Spin polarization of conduction electrons induced by electric current in two-dimensional asymmetric electron systems, *Solid State Commun.* **73**, 233 (1990).
- [25] E. Saitoh, M. Ueda, H. Miyajima, and G. Tatara, Conversion of spin current into charge current at room temperature: Inverse spin-Hall effect, *Appl. Phys. Lett.* **88**, 182509 (2006).
- [26] S. O. Valenzuela and M. Tinkham, Direct electronic measurement of the spin Hall effect, *Nature (London)* **442**, 176 (2006).
- [27] W. Zhang, M. B. Jungfleisch, W. Jiang, J. E. Pearson, and A. Hoffmann, Spin pumping and inverse Rashba-Edelstein effect in  $\text{NiFe/Ag/Bi}$  and  $\text{NiFe/Ag/Sb}$ , *J. Appl. Phys.* **117**, 17C727 (2015).
- [28] M. Isasa, M. C. Martínez-Velarte, E. Villamor, C. Magén, L. Morellón, J. M. De Teresa, M. R. Ibarra, G. Vignale, E. V. Chulkov, E. E. Krasovskii, L. E. Hueso, and F. Casanova, Origin of inverse Rashba-Edelstein effect detected at the  $\text{Cu/Bi}$  interface using lateral spin valves, *Phys. Rev. B* **93**, 014420 (2016).
- [29] S. Vélez, V. N. Golovach, A. Bedoya-Pinto, M. Isasa, E. Sagasta, M. Abadia, C. Rogero, L. E. Hueso, F. S. Bergeret, and F. Casanova, Hanle magnetoresistance in thin metal films with strong spin-orbit coupling, *Phys. Rev. Lett.* **116**, 016603 (2016).
- [30] H. Nakayama, M. Althammer, Y.-T. Chen, K.-I. Uchida, Y. Kajiwara, D. Kikuchi, T. Ohtani, S. Geprägs, M. Opel, S. Takahashi, R. Gross, G. E. W. Bauer, S. T. B. Goennenwein, and E. Saitoh, Spin Hall magnetoresistance induced by a nonequilibrium proximity effect, *Phys. Rev. Lett.* **110**, 206601 (2013).
- [31] N. Vlietstra, J. Shan, V. Castel, B. J. van Wees, and J. Ben Youssef, Spin-Hall magnetoresistance in platinum on yttrium iron garnet: Dependence on platinum thickness and in-plane/out-of-plane magnetization, *Phys. Rev. B* **87**, 184421 (2013).
- [32] P. He, S. S.-L. Zhang, D. Zhu, Y. Liu, Y. Wang, J. Yu, G. Vignale, and H. Yang, Bilinear magnetoelectric resistance as a probe of three-dimensional spin texture in topological surface states, *Nat. Phys.* **14**, 495 (2018).
- [33] P. He, C.-H. Hsu, S. Shi, K. Cai, J. Wang, Q. Wang, G. Eda, H. Lin, V. M. Pereira, and H. Yang, Nonlinear magnetotransport shaped by Fermi surface topology and convexity, *Nat. Commun.* **10**, 1290 (2019).
- [34] D. MacNeill, G. Stiehl, M. Guimarães, R. Buhrman, J. Park, and D. Ralph, Control of spin-orbit torques through crystal symmetry in  $\text{WTe}_2$ /ferromagnet bilayers, *Nat. Phys.* **13**, 300 (2017).
- [35] See Supplemental Material at <http://link.aps.org/supplemental/10.1103/PhysRevB.108.165407> for supplemental data, as well as an overview of electronic structures of  $\text{WTe}_2$ , including Refs. [33,43–51].
- [36] L. Cornelissen, J. Liu, R. Duine, J. B. Youssef, and B. van Wees, Long-distance transport of magnon spin information in a magnetic insulator at room temperature, *Nat. Phys.* **11**, 1022 (2015).
- [37] F. L. Bakker, A. Slachter, J.-P. Adam, and B. J. van Wees, Interplay of Peltier and Seebeck effects in nanoscale nonlocal spin valves, *Phys. Rev. Lett.* **105**, 136601 (2010).
- [38] T. Liu, J. Peiro, D. K. de Wal, J. C. Leutenantsmeyer, M. H. D. Guimarães, and B. J. van Wees, Spin caloritronics in a  $\text{CrBr}_3$ -based magnetic van der Waals heterostructure, *Phys. Rev. B* **101**, 205407 (2020).
- [39] X. Yang, C. H. van der Wal, and B. J. van Wees, Detecting chirality in two-terminal electronic nanodevices, *Nano Lett.* **20**, 6148 (2020).
- [40] A. Roy, M. H. D. Guimarães, and J. Sławińska, Unconventional spin Hall effects in nonmagnetic solids, *Phys. Rev. Mater.* **6**, 045004 (2022).
- [41] P. Li, C. Zhang, Y. Wen, L. Cheng, G. Nichols, D. G. Cory, G.-X. Miao, and X.-X. Zhang, Anisotropic planar Hall effect in the type-II topological Weyl semimetal  $\text{WTe}_2$ , *Phys. Rev. B* **100**, 205128 (2019).
- [42] H. Jafari, A. Roy, and J. Sławińska, Ferroelectric control of charge-to-spin conversion in  $\text{WTe}_2$ , *Phys. Rev. Mater.* **6**, L091404 (2022).
- [43] W.-D. Kong, S.-F. Wu, P. Richard, C.-S. Lian, J.-T. Wang, C.-L. Yang, Y.-G. Shi, and H. Ding, Raman scattering investigation of large positive magnetoresistance material  $\text{WTe}_2$ , *Appl. Phys. Lett.* **106**, 081906 (2015).
- [44] M. B. Nardelli, F. T. Cerasoli, M. Costa, S. Curtarolo, R. De Gennaro, M. Fornari, L. Liyanage, A. R. Supka, and H. Wang, PAOFLOW: A utility to construct and operate on *ab initio* Hamiltonians from the projections of electronic wavefunctions on atomic orbital bases, including characterization of topological materials, *Comput. Mater. Sci.* **143**, 462 (2018).
- [45] F. T. Cerasoli, A. R. Supka, A. Jayaraj, M. Costa, I. Siloi, J. Sławińska, S. Curtarolo, M. Fornari, D. Ceresoli, and M. B. Nardelli, Advanced modeling of materials with PAOFLOW 2.0: New features and software design, *Comput. Mater. Sci.* **200**, 110828 (2021).
- [46] A. Mar, S. Jobic, and J. A. Ibers, Metal-metal vs tellurium-tellurium bonding in  $\text{WTe}_2$  and its ternary variants  $\text{TaIrTe}_4$  and  $\text{NbIrTe}_4$ , *J. Am. Chem. Soc.* **114**, 8963 (1992).
- [47] S. Grimme, J. Antony, S. Ehrlich, and H. Krieg, A consistent and accurate *ab initio* parametrization of density functional dispersion correction (DFT-D) for the 94 elements H-Pu, *J. Chem. Phys.* **132**, 154104 (2010).
- [48] P. Giannozzi, S. Baroni, N. Bonini, M. Calandra, R. Car, C. Cavazzoni, D. Ceresoli, G. L. Chiarotti, M. Cococcioni, I. Dabo, A. Dal Corso, S. de Gironcoli, S. Fabris, G. Fratesi, R. Gebauer, U. Gerstmann, C. Gougoussis, A. Kokalj, M. Lazzeri, L. Martin-Samos *et al.*, QUANTUM ESPRESSO: a modular and open-source software project for quantum simulations of materials, *J. Phys.: Condens. Matter* **21**, 395502 (2009).

- [49] P. Giannozzi, O. Andreussi, T. Brumme, O. Bunau, M. B. Nardelli, M. Calandra, R. Car, C. Cavazzoni, D. Ceresoli, M. Cococcioni, N. Colonna, I. Carnimeo, A. Dal Corso, S. de Gironcoli, P. Delugas, R. A. DiStasio Jr., A. Ferretti, A. Floris, G. Fratesi, G. Fugallo *et al.*, Advanced capabilities for materials modelling with Quantum ESPRESSO, *J. Phys.: Condens. Matter* **29**, 465901 (2017).
- [50] J. P. Perdew, K. Burke, and M. Ernzerhof, Generalized gradient approximation made simple, *Phys. Rev. Lett.* **77**, 3865 (1996).
- [51] K. S. Novoselov, A. K. Geim, S. V. Morozov, D.-e. Jiang, Y. Zhang, S. V. Dubonos, I. V. Grigorieva, and A. A. Firsov, Electric field effect in atomically thin carbon films, *Science* **306**, 666 (2004).